Investigating the microstructure of a yield-stress fluid by light scattering

David Lee,[1] Iris A. Gutowski,[1] Arthur E. Bailey,[2] Laurent Rubatat,[1,3] John R. de Bruyn,[4] and Barbara J. Frisken[1,*]

[1]*Department of Physics, Simon Fraser University, Burnaby, British Columbia, Canada, V5A 1S6*
[2]*Scitech Instruments Inc., North Vancouver, British Columbia, Canada, V7J 2S5*
[3]*IPREM/EPCP, Université de Pau et des Pays de l' Adour, F-64053 Pau, France*
[4]*Department of Physics and Astronomy, University of Western Ontario, London, Ontario, Canada, N6A 3K7*

We report the results of an experimental study of the microstructure of dispersions of Carbopol ETD 2050, a model yield-stress fluid. Using two different light scattering instruments, measurements were made over three decades in scattering wave vector, from 0.02 to 25 μm^{-1}. These measurements reveal microstructure characterized by two length scales: a longer length scale, 6 μm and larger, that depends on Carbopol concentration and the pH of the dispersion and a shorter length scale of approximately 400 nm that is independent of both sample concentration and pH. We relate these results to shear rheology measurement of the yield stress of these materials.

　　　　　　PACS number(s): 83.80.Kn, 83.60.La, 82.70.Gg

I. INTRODUCTION

The defining characteristic of yield-stress fluids is their ability to flow only if sufficient shear stress is applied. Below this yield stress they behave as soft elastic solids but above the yield stress their response includes both dissipation and storage of energy. Recent work distinguishes between simple yield-stress materials, such as Carbopol, emulsions, and foams, in which the shear stress depends only on the shear rate, and thixotropic materials, such as Laponite clay suspensions and colloidal gels, in which the flow behavior and shear stress depend on the shear history [1]. As is the case with all soft materials, the properties of yield-stress fluids depend on the presence of structure larger than the individual molecules but smaller than the bulk material. However, there is little understanding of the relationship between the microscopic structure of yield-stress fluids and their macroscopic behavior [2].

Carbopol, a family of synthetic, high-molecular-weight, cross-linked, acrylic acid-based polymers, is a thickener used extensively in personal care, household, and industrial products. It is typically provided as a powder with grains a few micrometers in size, which swell when dispersed in water. Unmodified aqueous dispersions of Carbopol are acidic because of the presence of a carboxyl group on the polymer backbone. When the pH of the samples is increased by adding a base such as sodium hydroxide, the grains swell extensively, by up to a factor of 10 in diameter or 1000 in volume [3]. As they swell, the particles jam and form a soft colloidal paste, typical of simple yield-stress materials [1,4]. Carbopol gels are used as model yield-stress fluids because they are transparent [5,6], making them well suited to optical flow-visualization experiments and because their rheological properties can be tuned by varying the pH and concentration of the sample [7,8].

Beyond characterizing the dependence of rheological properties on sample parameters, several studies aimed at understanding the microstructural basis of these properties have been published. Carnali and Naser [9] used dilute-solution

viscometry to reveal behavior consistent with microgel particles that swell enormously on hydration and to determine the crosslink density and shear modulus of the microgel dispersion. Light scattering [10] and particle-tracking microrheology [4,10,11] have been used to study the micron-scale structure of Carbopol. The microrheological measurements show that pH-6 Carbopol dispersions are inhomogeneous over a range of concentrations. For concentrations above that at which a bulk yield stress becomes measurable, two distinct microrheological environments are observed, one primarily viscous and the other primarily elastic, with the volume fraction of the elastic environment increasing with the Carbopol concentration [4]. The microrheology experiments show that the onset of a bulk yield stress is associated with jamming of the microgel particles on a microscopic scale [4]. Attempts at more direct observation of microstructure have included cryogenic scanning electron microscopy (SEM) studies [12], which show honeycomb-like structures with a length scale of order 5 μm independent of Carbopol concentration. It has been suggested, however, that this structure may be an artifact of the method by which the SEM samples were prepared [13]. Because the swelling of the Carbopol particles is so extensive, Carbopol dispersions are transparent and the microstructure is not easily studied by optical microscopy [13]. Recent static light scattering measurements on Carbopol 940 samples reveal some structure on length scales of about 1 μm [13].

In this paper we report static light scattering measurements on Carbopol dispersions performed over an extended range of scattering wave vectors obtained by use of two instruments: a custom built small-angle light scattering (SALS) instrument based on detection using a CCD camera and a wider-angle commercial instrument based on detection using a photomultiplier tube. The detection unit of our home-built SALS instrument is mounted off axis to reduce lens abberation, resulting in near diffraction-limited performance. Using these two instruments we are able to measure scattering wave vectors q ranging from 0.02 to 25 μm^{-1}; over three orders of magnitude. We report the results of measurements on Carbopol ETD 2050 dispersions performed over a wide range of concentrations and pH. We relate our light scattering results to shear rheology measurements of the yield stress.

―――――――
*frisken@sfu.ca

II. EXPERIMENT

A. Sample preparation

We used Carbopol ETD 2050, an easy-to-disperse version of Carbopol 941, in these experiments [3]. The *p*Ka of acrylic acid is 4.25 while the *p*Ka of Carbopol is reported to be 6.0 ± 0.5. Its molar mass is not well known, but it has been estimated to be in the range of 1–4 GDa [3]. A 5 wt% Carbopol dispersion was prepared by adding the appropriate amount of Carbopol ETD 2050 powder to distilled deionized water over the course of several hours, while stirring at roughly 100 rpm with a magnetic stir bar. The sample was stirred for an additional 12 hours at approximately 50 rpm to ensure that the particles were homogeneously dispersed and had reached their equilibrium size [14–16]. This dispersion was then diluted to produce samples with concentrations *c* of 2.0, 1.5, 1.0, 0.5, 0.2, and 0.1 wt%, which had *p*H values ranging from 2.5 to 3.6, depending on the polymer concentration. A higher polymer concentration results in a higher concentration of carboxylic acid groups and, therefore, a lower *p*H. We refer to these samples as *p*H-unmodified samples.

Each of these samples was divided into 8–10 smaller samples. 20 wt% aqueous sodium hydroxide (NaOH) was added to obtain samples with *p*H values ranging up to 11. Concentrated NaOH was used to minimize the dilution during *p*H adjustment. After the NaOH was added, the samples were stirred slowly as the *p*H equilibrated. The final *p*H of each sample was typically measured 15 hours after addition of the NaOH. These are referred to as *p*H-modified samples.

B. Static light scattering

Light is scattered by local variations of the dielectric constant within the sample that result from variations in density or concentration [17]. Static light scattering (SLS) measures the intensity of the scattered light relative to the incident intensity as a function of the scattering angle θ. This ratio, $S(q)$, is a function of the magnitude of the scattering wave vector $q = (4\pi n/\lambda_0) \sin(\theta/2)$, where n is the refractive index of the scattering medium and λ_0 is the wavelength of the incident light in vacuum. Our static light scattering measurements were performed using two instruments: a small-angle light scattering instrument and a commercial light scattering instrument, ALV-5000/ e DLS/SLS (ALV-Gmbh). This combination provides scattering angles ranging from 0.08 to 150 degrees, which translates into a scattering q range of 0.02 to 25 μm^{-1} when using a helium-neon laser with $\lambda_0 = 632.8$ nm. Since scattering at a given q corresponds to scattering from fluctuations in the dielectric constant of size $\xi \approx 1/q$, this angular range represents a range of length scales $0.04 < \xi < 50$ μm. All measurements were performed at room temperature.

1. Small-angle light scattering instrument

The SALS instrument consists of three major components: a laser source with beam expander, a sample platform, and a detection system. The small-angle light scattering instrument uses a CCD camera to detect the scattered light over a two-dimensional (2D) array of pixels, allowing simultaneous measurement at angles ranging from 0.08 to 10 degrees [18]. Figure 1 is a schematic of the instrument.

The incident laser beam passes through a Keplerian beam expander and spatial filter combination before passing through the sample. This ensures that the beam cross section remains circular and Gaussian and expands the beam to a diameter, approximately 3 mm, that will result in scattered speckles smaller than the CCD pixel size after accounting for the magnification of the detection optical system. The sample holder is centered on the incident beam. Samples are loaded into cylindrical cells with optical windows at each end, oriented with the cylindrical axis coaxial with the optical axis. The detection system houses the collection optics, camera optics, and a CCD camera. All items in the detection system are optically aligned with the center of the cell. The entire detection system is oriented at an angle Ψ relative to the
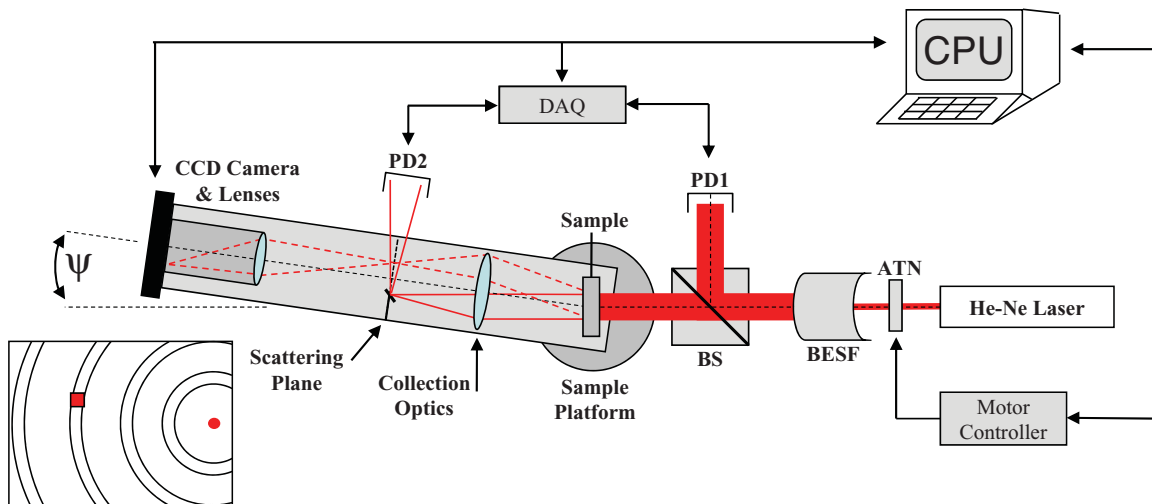

FIG. 1. (Color online) Schematic of the small-angle light scattering instrument setup used in these experiments. Components are described in the text. The lower left shows the field of view seen by the camera. The solid circle represents the optical center and the solid square represents the size of a CCD pixel relative to one of the concentric rings of constant scattering angle θ. ATN: Attenuator, PD: Photodiode, BS: Beam splitter, BESF: Beam expander and spatial filter.

transmitted beam, which is approximately half the maximum measurable angle. This results in substantially reduced optical aberrations and improved performance near the diffraction limit across the entire field of view or range of scattering angles. A very small polished mirror is placed at the location of the focused beam in the scattering plane to divert the strong transmitted beam to a photodiode. Vignetting of the scattered light was eliminated by optically conjugating the sample cell very near the entrance pupil of the camera lens [19].

All optical surfaces were treated with antireflective coatings, and all mounts and enclosures were anodized flat black to minimize stray light. Measurements made with a sample containing solvent only are used to correct sample measurements for the excess scattering from the solvent background and from stray-light sources.

Using multiple exposure times and ensuring that data was acquired only within the linear response of the CCD camera, we found that the dynamic range of the instrument was effectively extended to at least 8.4 decades.

A static light scattering measurement of the average intensity as a function of scattering angle is performed by calculating the azimuthal average over the two-dimensional CCD plane of all pixels belonging to the same scattering angle. We use LabView to calculate the relative intensity of light scattered from the sample and to correct for contributions from solid angle, polarization, turbidity, and sample scattering length [19].

2. Traditional light scattering instrument

A commercial light scattering instrument (ALV-5000/eDLS/SLS, ALV-Gmbh) equipped with a goniometer and a photomultiplier tube was used for traditional light scattering (SLS) measurements of the scattered intensity of the Carbopol samples over an angular range of $13°$ to $150°$.

Carbopol gels exhibit nonergodic behavior, meaning that time averaging fails to fully represent the ensemble average. To generate a proper ensemble average, the cuvette was rotated for all samples for static light scattering measurements performed in the ALV instrument [20].

3. Analysis of scattering results

We analyzed our light scattering data by fitting it to a structure factor consistent with fractal or aggregate systems. In general, our samples are weak scatterers and, even though some of the structure is larger than the wavelength of light, the phase shift is small. As a result, all analysis can be performed in the Rayleigh, or Rayleigh-Debye, limit [21]. In this case, the structure factor $S(q)$ is the Fourier transform of the correlation function $G(r)$.

For fractal systems, the mass distribution of the object is described as $M(r) \propto r^{D_f}$, where r is the distance from an arbitrary origin to a scattering point in the object, and D_f is the fractal dimension. The density-density correlation function of the material can then be written as [22]

$$G(r) = Ae^{-r/\xi}r^{D_f - 3}, \qquad (1)$$

where A is a normalization constant and ξ is an upper cutoff length that describes the extent of the fractal region, since the cutoff function $e^{-r/\xi}$ is equal to 1 for $r \ll \xi$ and rapidly falls

to zero when $r \gg \xi$. For $G(r)$ given by Eq. (1),

$$S(q) = \frac{S(0)}{(1 + q^2\xi^2)^{(D_f-1)/2}} \frac{\sin[(D_f - 1)\tan^{-1}(q\xi)]}{(D_f - 1)q\xi}. \qquad (2)$$

At small q, $S(q) \rightarrow S(0)$ and is approximately constant, indicating that there are spatial fluctuations on all length scales. At large q, $S(q)$ falls off with power-law behavior, $S(q) \propto q^{-D_f}$. The transition between these two limits occurs at $q \approx 1/\xi$. This structure factor has been used to interpret scattering from many systems including silica aerogels [23], colloidal silica gels [24], and randomly crosslinked polymers [25], where the length scale ξ was interpreted as the correlation length, the finite size of fractal clusters, and the extent of polymer density fluctuations, respectively.

C. Rheology

Rheological measurements were performed using an ARES RHS strain-controlled rheometer with a cone and plate geometry. The cone was 5 cm in diameter and had a cone angle of 0.04 radians. Fine sandpaper was glued to the surfaces of the cone and plate to eliminate slip at the surface [7].

The yield stress τ_y for each sample was obtained by measuring the flow curve; that is, the steady-state shear stress τ as a function of the applied shear rate $\dot{\gamma}$. The yield stress of each sample was determined by fitting the Herschel-Bulkley model,

$$\tau = \tau_y + K\dot{\gamma}^n, \qquad (3)$$

to the data, where the yield stress τ_y, the consistency or plastic viscosity K, and the power-law exponent n were used as fit parameters [26].

III. RESULTS

A. Rheology

Flow curves were measured for the full range of concentrations and pH [27]. As an example, the flow curve for $c = 1$ wt% Carbopol at pH $= 3.83$ is shown in Fig. 2, along with a fit of the Herschel-Bulkley model, Eq. (3), to the data. The model provides an excellent description of the data in this and all other cases where the yield stress was measurable.

Figure 3 displays the yield stress obtained for each Carbopol sample plotted as a function of pH. For a given Carbopol concentration the yield stress increases with pH, reaches a maximum, and then decreases slightly. The maximum yield stress increases with increasing concentration and occurs at a lower pH for samples of larger Carbopol concentration. For example, the maximum yield stress occurs at pH $= 7$ for a $c = 0.5$ wt% sample as compared to pH $= 4$ for $c = 2.0$ wt%.

B. Light scattering

Figure 4 shows the scattered light intensity relative to the incident intensity, $S(q)$, for Carbopol samples with $c = 1.0$ wt% and pH ranging from 2.83 to 10.98. Data from both scattering instruments are presented for each sample, where data in the range from $0.02 < q < 2$ μm^{-1} were taken with the SALS instrument and the data in the range from
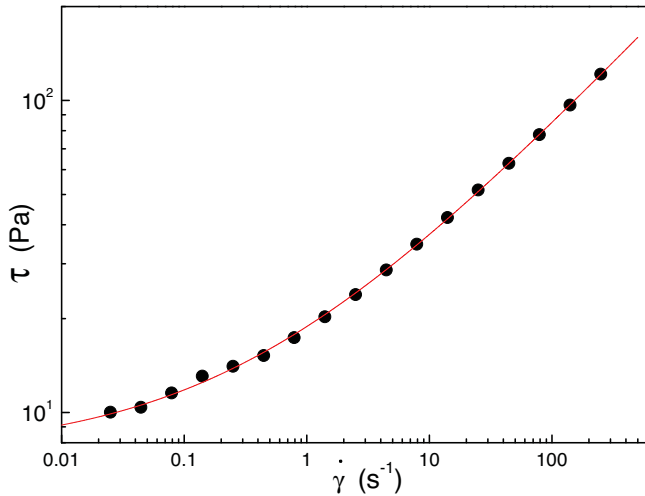
FIG. 2. (Color online) Shear stress as a function of shear rate measured for $c = 1.0$ wt% Carbopol sample at pH 3.83. The curve is a fit to the Herschel-Bulkley model, Eq. (3), with $\tau_y = 7.4 \pm 0.2$ Pa, $K = 11.4 \pm 0.2$ Pa s^n, and $n = 0.416 \pm 0.003$.

$3 < q < 25$ μm^{-1} were obtained with the SLS instrument. The amount of light collected by each apparatus depends on the geometry of the system as well as the turbidity of the sample. The geometrical factor was determined by matching the scattering curves obtained from the two instruments for the lowest-pH sample of each concentration series. The data from both instruments were also corrected for the turbidity, which was measured using the SALS instrument.

In general, the scattered intensity decreases monotonically as the pH is increased, with larger drops in intensity observed in the small-q region of the data. Two features can be identified in the data, as indicated by arrows in Fig. 4. In the sample with the lowest pH, the scattering intensity shows a change in slope at a wave vector $q_1 \approx 0.1$ μm^{-1} (down arrow), corresponding to a length scale $\xi_1 \approx 1/q_1 \approx 10$ μm, and decreases with a
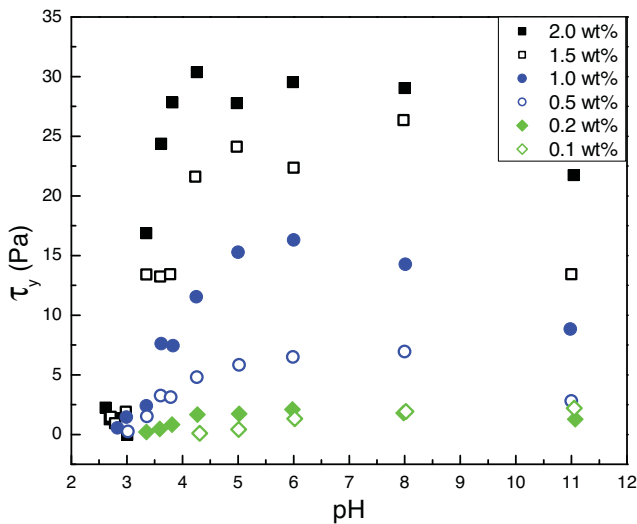

FIG. 3. (Color online) Yield stress as a function of pH for Carbopol concentrations ranging from $c = 0.1$ wt% to $c = 2.0$ wt%. The different symbols indicate different concentrations.
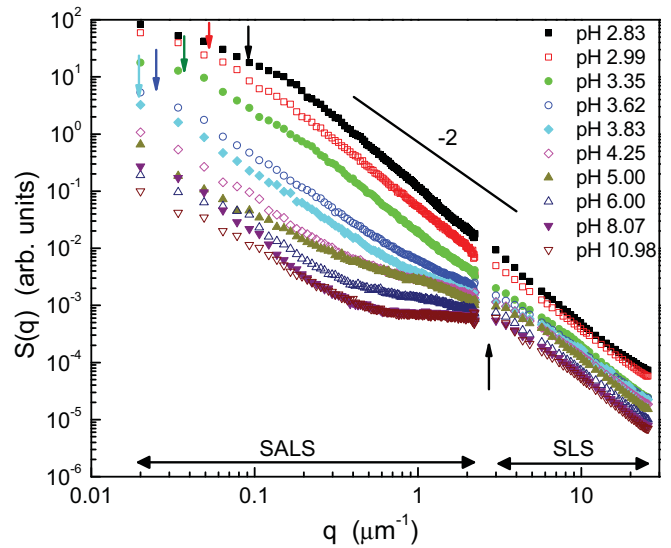

FIG. 4. (Color online) Relative intensity of the scattered light $S(q)$ as a function of scattering wave vector q for 1 wt% Carbopol ETD 2050 and a range of pH values. The arrows identify the locations of the two main scattering features as discussed in the text.

power-law dependence on q for $q > q_1$. This feature moves to lower q as the pH is increased, and cannot be observed for pH > 4. In the higher-pH samples, the scattered intensity shows a second change in slope at $q_2 = 1/\xi_2 \approx 0.4$ μm (up arrow) then again shows a power-law decrease for $q > q_2$. From Fig. 4, ξ_2 appears to be pH-independent, although its contribution to the scattering becomes more obvious as the pH is increased.

The low-pH data can be successfully modeled by a function consisting of a sum of two terms of the form given by Eq. (2):

$$S(q) = S_1(q) + S_2(q), \tag{4}$$

characterized by parameters $S_1(0)$, ξ_1, and D_{f1} and $S_2(0)$, ξ_2, and D_{f2}, respectively. For pH values above 4, the small-q feature is not always evident. In modeling these data, we made the assumption that ξ_1 is too large to be measured by our SALS instrument. $S_1(q)$ was thus replaced by a simpler function $F_1(q) = F(0)q^{-D_{f1}}$, in which case $S(q)$ is written as

$$S(q) = F_1(q) + S_2(q). \tag{5}$$

A fit of Eq. (4) to the data for 0.1 wt% Carbopol at pH $= 3.81$ is shown in Fig. 5. The top panel shows the data along with three curves: the curve given by Eq. (4) and two curves representing each of the two terms in this function. Arrows on this figure identify the characteristic length scales obtained from the fits, and lines represent the slopes of the high-q power laws from each term in Eq. (4). The bottom panel shows the residuals of the fit, presented in units of the uncertainty of the data.

Figure 6 displays the results for the characteristic length scales ξ_1 and ξ_2 as determined from fits of Eqs. (4) or (5), as appropriate, to the data. The characteristic length scale ξ_1 of the pH-unmodified samples (i.e., those with no base added) increases with concentration from 6.0 ± 0.1 μm at $c = 0.1$ wt% to 23.1 ± 0.3 μm at $c = 2.0$ wt%. For each concentration, increasing the pH results in a larger ξ_1. Around
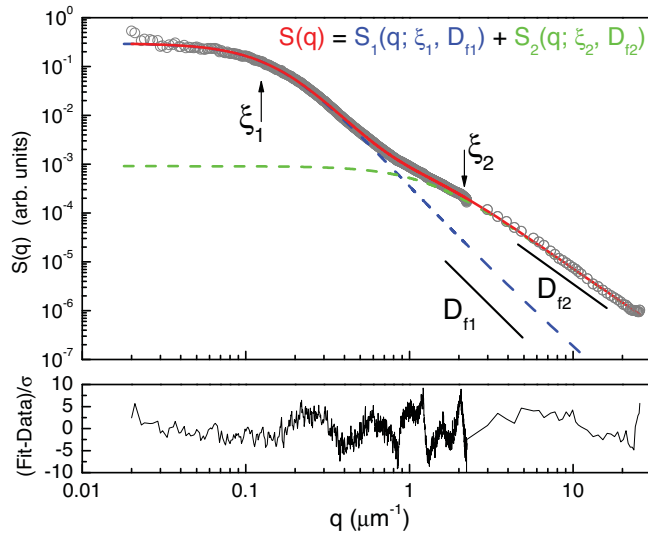
FIG. 5. (Color online) Fit of Eq. (4) to the light scattering data for 0.1 wt% Carbopol at $pH = 3.81$. The data are shown as open circles, and the three curves show $S_1(q)$, $S_2(q)$, and their sum $S(q)$. The residuals, in units of the data uncertainty, are shown in the lower portion of the figure.

$pH = 4$, ξ_1 increases to the point where it is too large to measure. The second characteristic length scale, ξ_2, appears to be roughly constant over the concentration and pH range studied, although there is some scatter in ξ_2 at low pH. The horizontal lines in Fig. 6(b) show the weighted mean and the standard deviation of the distribution of ξ_2, calculated for samples with $pH > 4$. The mean value is 0.42 μm and the standard deviation is 0.05 μm.

Figure 7 shows the fractal dimensions D_{f1} and D_{f2}. Both are scattered between 2.0 and 2.5 over most of the concentration and pH range, except for $pH \leqslant 4$ where several larger values for D_{f1} were measured. In particular, the fractal dimension D_{f1} for the lowest-concentration pH-unmodified sample, shown as an encircled open diamond, is 3.0; other low-concentration and pH-unmodified samples have fractal dimensions D_{f1} that decrease as the concentration increases. The lines in Figs. 7(a) and 7(b) show the weighted mean and the standard deviation of the distributions of D_{f1} and D_{f2}, respectively, calculated for samples with $pH > 4$. We find means and standard deviations of 2.28 ± 0.10 and 2.28 ± 0.06 for D_{f1} and D_{f2}, respectively.

Preliminary small-angle neutron scattering (SANS) data show that the high-q power-law behavior observed in the light scattering experiments persists down to length scales as small as 1 nm. Figure 8 shows SANS data obtained on a sample of 1.5 wt% Carbopol ETD 2050 at pH 6, prepared in D_2O to provide contrast for neutron scattering. The data were obtained using the NG7-30-m SANS instrument at the NIST Center for Neutron Research (Gaithersburg, MD). Light scattering data for a sample with the same concentration and pH, but prepared with H_2O (as usual) are also shown. The SANS data are in excellent agreement with the light scattering data in the overlap region and show the same power-law slope, corresponding to a fractal dimension of approximately 2.3, over an additional two orders of magnitude in q.
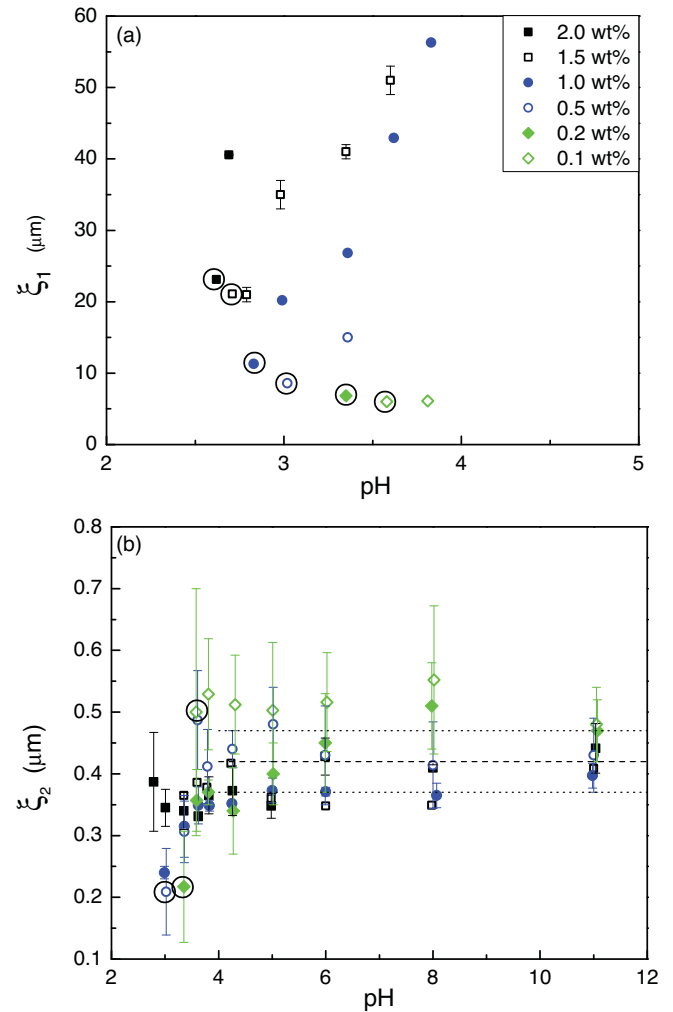

FIG. 6. (Color online) The characteristic length scales (a) ξ_1 and (b) ξ_2 plotted as a function of pH for a range of Carbopol concentrations. The encircled markers represent data from pH-unmodified Carbopol samples. The horizontal lines in (b) represents the weighted mean and standard deviation of the data for $pH \geqslant 4$. Error bars smaller than the data markers are not shown.

IV. DISCUSSION

The light scattering data can be successfully modeled by a sum of two fractal structure functions, each with a long-range cutoff. The longer length scale (small-q) contribution decreases in intensity as the pH of the samples is increased. The corresponding length scale ξ_1 increases to the point where it is too large to measure with our instrument. The shorter length scale ξ_2 associated with the large-q contribution does not change significantly over the pH and concentration range studied. The fractal dimension D_{f1} of the small-q component decreases from roughly 3 to about 2.3; the fractal dimension D_{f2} is 2.3 in all samples measured. Preliminary SANS experiments show that this fractal dimension persists to length scales as small as 1 nm.

The growth of the longer length scale ξ_1, decrease in the fractal dimension D_{f1}, and reduced scattering at low q are consistent with swelling of the particles as the pH is increased. The relationship between ξ_1 and D_{f1} is shown in Fig. 9 for
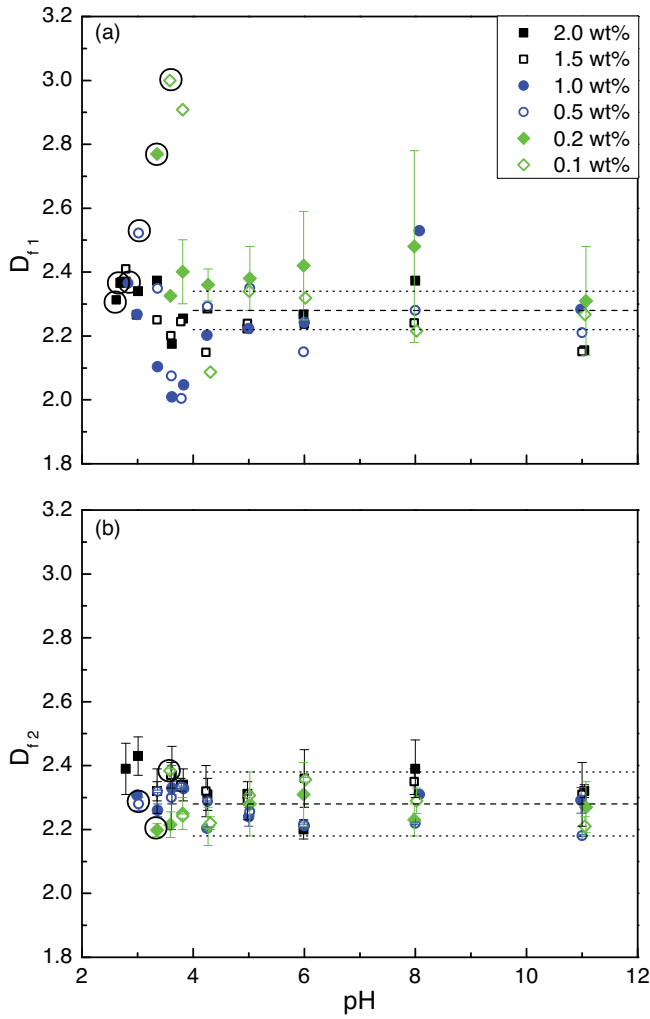
FIG. 7. (Color online) The pH dependence of the fractal dimensions (a) D_{f1} and (b) D_{f2} for samples of different Carbopol concentration. The encircled markers represent data from pH-unmodified Carbopol samples. The dashed and dotted horizontal lines represents the weighted mean and standard deviation of the data for samples with $pH \geqslant 4$.

all samples having $\xi_1 < 25$ μm. ξ_1 was approximately 6 μm for the lowest-concentration sample, with a corresponding fractal dimension $D_{f1} \simeq 3$, consistent with a space-filling object. In this case ξ_1 must be a measure of the diameter of the hydrated, but largely unswollen particles, consistent with the manufacturer's description of Carbopol as a hydrated resin averaging 0.8–12 microns in diameter [3]. As the pH of the dispersion is increased to about 4, ξ_1 quickly exceeds the largest measurable size, which is limited to about 50 μm by the current configuration of the SALS instrument, and D_{f1} decreases to about 2.3, consistent with the fractal dimension of a randomly branched polymer [28]. We did not observe a subsequent decrease in ξ_1 or a change in D_{f1} at very high pH.

Figure 6(a) also shows that, as the concentration of pH-unmodified samples is increased, ξ_1 also increases. As the pH of these samples is decreasing, this is contrary to the general growth in ξ_1 with increasing pH for samples of the same concentration. We can offer no explanation for this behavior at this time.
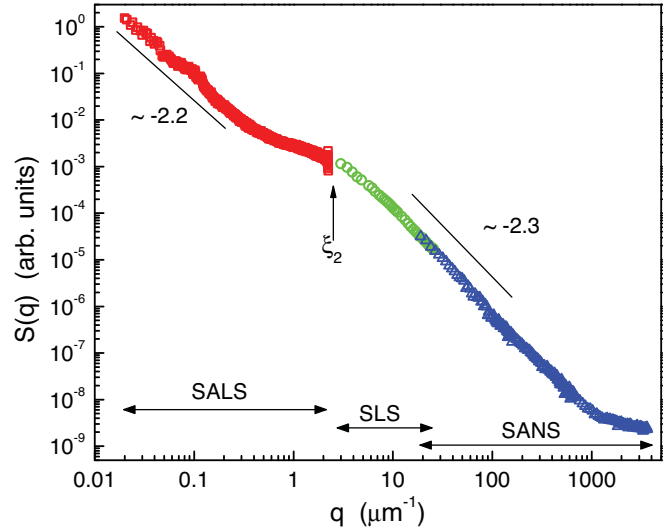

FIG. 8. (Color online) Small-angle neutron scattering and light scattering data for Carbopol with $c = 1.5$ wt% Carbopol sample adjusted to $pH = 6.0$.

The length scale ξ_2 and fractal dimension D_{f2} associated with the higher-q contribution to the structure function show little variation over the entire concentration and pH range. This suggests that there are regions within the polymer that do not swell, perhaps because the polymer in these regions is more heavily crosslinked. These unswollen regions are revealed as the contrast between the swelling polymer and the solvent decreases. The data appear to be consistent with a length scale ξ_2 that describes the size of the regions, rather than their separation [29].

Crosslinking constrains the polymer from undergoing uncontrolled expansion. Lightly crosslinked polymers expand easily, while heavily crosslinked polymers expand only slightly or not at all. Randomly crosslinked polymers are
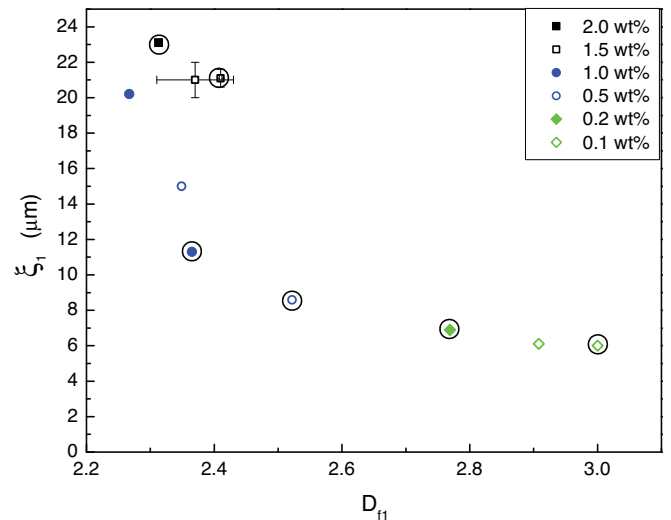

FIG. 9. (Color online) Correlation between the longer length scale ξ_1 and the corresponding fractal dimension D_{f1}. As the particles swell, the fractal dimension decreases from 3 to 2.3. The encircled markers represent data from pH-unmodified Carbopol samples.

typically heterogeneous, with regions of higher- and lower-than-average crosslink density [30]. Alternately, the difference in crosslink density may result from the synthesis process where rapid consumption of the crosslinker may lead to a lower crosslink concentration in the outer regions of the polymer network. Crosslinked poly-N-isopropylacrylamide (poly-NIPAM) particles show regions of higher density that have been attributed to this effect, and that have been successfully modeled as having a denser core and a less-dense outer halo [31,32]. Small-angle neutron scattering measurements of a dilute dispersion of poly-NIPAM by Mason and Lin [32] show the existence of two radii, ascribed by them to a core and an outer region. Their measurements show that, when the temperature is raised above the polymer's coil-globule transition temperature, the radius of the outer region decreases to approximately the radius of the inner core. They found their data to be consistent with the polymer density being constant within the core of the microgel particle and decreasing linearly to zero at the outer radius. The size of the inner core was determined to be approximately 175 nm, independent of temperature. However, the largest radius measured for the swollen poly-NIPAM microgel particles was 350 nm, yielding a size ratio of just a factor of two. By comparison, the ratio of ξ_1/ξ_2 found here ranges from 15 to over 100. Fits using the core-shell model of Ref. [32] did not describe our data. On the other hand, the excellent agreement between the data and our fitting function consisting of two independent terms supports the idea of random heterogeneities rather than a core-shell structure.

Our measurements of the microstructure of Carbopol are consistent with the yield stress of this material being a result of dense packing or jamming of soft particles [1,4]. The scattering results show that the samples are made up of randomly crosslinked polymer microgels that swell dramatically over the same pH range at which the yield stress is observed to increase. Swelling by at least a factor of 10 in size or 1000 in volume means that jamming, leading to a yield stress, can occur in very dilute samples. The pH dependence of the onset in the yield stress for each concentration is consistent with jamming of more concentrated samples occurring at lower degrees of swelling.

In fact there is an interesting correlation between the yield stress and the length scale ξ_1 when τ_y is relatively small, as shown in Fig. 10. The data in this figure correspond to the lower-left corner of Fig. 3 and the lower half of Fig. 6(a). The yield stress becomes measurable once ξ_1 becomes larger than about 6 μm and increases more-or-less linearly with ξ_1 over the range plotted. τ_y is a bulk quantity, while ξ_1 is related to the microstructure of the material, so the observed relationship hints at a connection between the two scales. While we do not completely understand the details of the interdependence of yield stress, concentration, pH, and ξ_1, these data are consistent with the picture developed in Ref. [4] that a bulk yield stress develops when the Carbopol particles expand to the extent that they become kinetically arrested due to jamming. A further swelling of the particle size results in stronger jamming and an increase in both elasticity and yield stress.

The yield stress of our Carbopol dispersions is observed to decrease at high pH values, consistent with the results of other authors [8]. This has been attributed to a de-swelling of
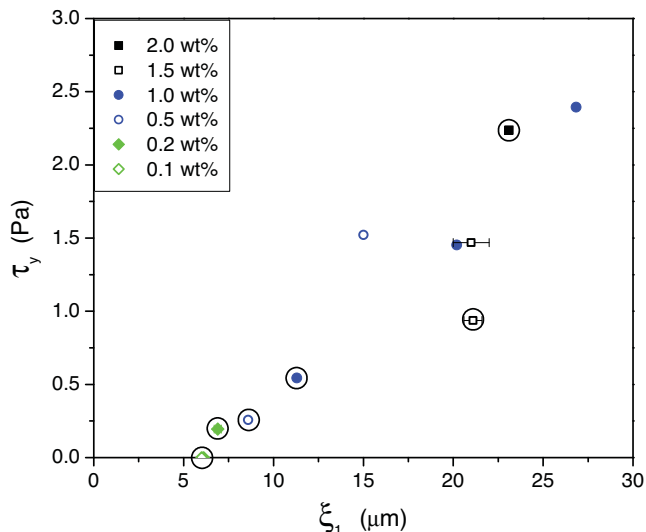

FIG. 10. (Color online) τ_y plotted as a function of ξ_1 for samples with low yield stress. The yield stress τ_y increases dramatically as the particles swell. Encircled data points identify pH-unmodified samples.

the Carbopol microgels due to excess ions [3]. A reduction in the ionic osmotic pressure should occur when the pH of the system is raised beyond that necessary for total ionization of the carboxylic groups of Carbopol. The contributions to the total osmotic pressure from mixing, configuration, and ions determine the swelling and de-swelling behavior of the polymer [30,33,34]. However, we do not observe any evidence of a decrease of particle size up to the highest pH measured; pH $= 11$. The turbidity of the samples continues to decrease as pH is increased for all pH measured; there is little consistent increase in scattering at small angles as might be expected due to increased contrast due to de-swelling; and there is no consistent signature for a decrease of ξ_1. Instead of decreased microgel size, the decrease in yield stress at high pH may occur because the highly expanded microgel particles are less elastic.

V. CONCLUSION

We have studied the microstructure of Carbopol ETD 2050. Using two different instruments, light scattering measurements were made over scattering wave vectors ranging from 0.02 to 25 μm^{-1}. These measurements reveal microstructure characterized by two length scales; a longer length scale ($\xi_1 > 6$ μm) that depends on Carbopol concentration and the amount of NaOH added, and a shorter length scale ($\xi_2 \approx 400$ nm) that is independent of sample properties.

The data were successfully modeled by a sum of two fractal structure functions each with a long-range cutoff. The longer-length-scale function decreases in intensity as the pH of the samples is increased and the corresponding length scale ξ_1 increases to the point where it is too large to measure with our instrument. This long length scale increases dramatically at the same pH at which the yield stress of the fluid increases. The shorter length scale ξ_2 does not change significantly over the pH and concentration range studied.

These results are consistent with scattering from microgel particles made up of randomly crosslinked polymers rather than particles consisting of heavily crosslinked cores decorated with dangling free ends as described in Ref. [7]. Most of the Carbopol swells substantially as the pH is changed, changing by over three orders of magnitude in volume. This larger region contains small regions (less than 1 part per million of the particle volume) that do not swell when the pH is increased, due to random heterogeneities in the crosslink density. The swelling of the Carbopol particles leads to jamming of these soft particles to form a soft paste, which is characterized by a concentration- and pH-dependent yield stress. While the yield stress decreases slightly in the samples with the highest pH, no evidence for shrinking of the particles was observed. The decrease in yield stress observed at high pH is more likely due to continued expansion and softening of the particles.

Carbopol's rheological behavior is close to that of an ideal yield-stress fluid [8], making it a useful model material on the macroscopic scale. Our results suggest that its microstructure, in contrast, is more complex than that of other microgels [31,32] and somewhat less than ideal. Nonetheless, we hope that this work will inspire additional studies by researchers intrigued by the relationship between microstructure and bulk properties in these materials.

[1] P. Moller, A. Fall, V. Chikkadi, D. Derks, and D. Bonn, Philos. Trans. R. Soc. London A **367**, 5139 (2009).

[2] P. Coussot, Soft Matter **3**, 528 (2007).

[3] Lubrizol Corporation, *Lubrizol Pharmaceutical Bulletins* (2002).

[4] F. K. Oppong and J. R. de Bruyn, Rheol. Acta (to be published).

[5] T. Toplak, H. Tabuteau, J. R. de Bruyn, and P. Coussot, Chem. Eng. Sci. **62**, 6908 (2007).

[6] A. M. V. Putz, T. I. Burghelea, I. A. Frigaard, and D. M. Martinez, Phys. Fluids **20**, 033102 (2008).

[7] G. P. Roberts and H. A. Barnes, Rheol. Acta **40**, 499 (2001).

[8] S. J. Curran, R. E. Hayes, A. Afacan, M. C. Williams, and P. A. Tanguy, J. Food Sci. **67**, 176 (2002).

[9] J. O. Carnali and M. S. Naser, Coll. Polym. Sci. **270**, 183 (1992).

[10] F. K. Oppong, L. Rubatat, B. J. Frisken, A. E. Bailey, and J. R. de Bruyn, Phys. Rev. E **73**, 041405 (2006).

[11] F. K. Oppong and J. R. de Bruyn, J. Non-Newt. Fluid Mech. **142**, 104 (2007).

[12] J.-Y. Kim, J.-Y. Song, E.-J. Lee, and S.-K. Park, Colloid Polym. Sci. **281**, 614 (2003).

[13] J. M. Piau, J. Non-Newt. Fluid Mech. **144**, 1 (2007).

[14] L. Baudonnet, D. Pere, P. Michaud, J.-L. Grossiord, and F. Rodriguez, J. Disper. Sci. Technol. **23**, 499 (2002).

[15] L. Baudonnet, J.-L. Grossiord, and F. Rodriguez, J. Disper. Sci. Technol. **25**, 183 (2004).

[16] H. Tabuteau, P. Coussot, and J. R. de Bruyn, J. Rheol. **51**, 125 (2007).

[17] R. Klein and B. D'Aguanno, *Light Scattering: Principle and Development* (Claredon Press, Oxford, 1996).

[18] D. Lee, M.S. thesis, Simon Fraser University, 2009.

[19] F. Ferri, Rev. Sci. Instrum. **68**, 2265 (1997).

[20] K. Schätzel, Adv. Colloid Interface Sci. **46**, 309 (1993).

[21] M. Kerker, *The Scattering of Light and Other Electromagnetic Radiation* (Academic Press, New York, 1969).

[22] S. K. Sinha, T. Freltoft, and J. K. Kjems, *Kinetics of Aggregation and Gelation* (North-Holland, Amsterdam, 1984).

[23] R. Vacher, T. Woignier, J. Pelous, and E. Courtens, Phys. Rev. B **37**, 6500 (1988).

[24] T. Freltoft, J. K. Kjems, and S. K. Sinha, Phys. Rev. B **33**, 269 (1986).

[25] A. N. Falcao, J. S. Pedersen, and K. Mortensen, Macromolecules **26**, 5350 (1993).

[26] J. W. Goodwin and R. W. Hughes, *Rheology for Chemists* (Royal Society of Chemistry, Cambridge, 2000).

[27] I. A. Gutowski, D. Lee, J. R. de Bruyn, and B. J. Frisken (unpublished).

[28] G. Beaucage, J. Appl. Crystallogr. **29**, 134 (1996).

[29] J. Bastide and S. J. Candau, *Physical Properties of Polymeric Gels* (Wiley, New York, 1974).

[30] A.-M. Hecht, R. Duplessix, and E. Geissler, Macromolecules **18**, 2167 (1985).

[31] A. Fernández-Barbero, A. Fernández-Nieves, I. Grillo, and E. López-Cabarcos, Phys. Rev. E **66**, 051803 (2002).

[32] T. G. Mason and M. Y. Lin, Phys. Rev. E **71**, 040801 (2005).

[33] E. Vasheghani-Farahani, J. H. Vera, D. G. Cooper, and M. E. Weber, Ind. Eng. Chem. Res. **29**, 554 (1990).

[34] B. R. Saunders and B. Vincent, *Encyclopedia of Surface and Colloid Science* (CRC, New York, 2002).